A Signal Processing Approach to Symmetry Detection

Yosi Keller and Yoel Shkolnisky

***Abstract*—We present an algorithm that detects rotational and reflectional symmetries of two-dimensional objects. Both symmetry types are effectively detected and analyzed using the angular correlation (AC), which measures the correlation between images in the angular direction. The AC is accurately computed using the pseudopolar Fourier transform, which rapidly computes the Fourier transform of an image on a near-polar grid. We prove that the AC of symmetric images is a periodic signal whose frequency is related to the order of the symmetry. This frequency is recovered via spectrum estimation, which is a proven technique in signal processing with a variety of efficient solutions. We also provide a novel approach for finding the center of symmetry and demonstrate the applicability of our scheme to the analysis of real images.**

I. Introduction

SYMMETRY detection and analysis is a fundamental task in computer vision. Naturally, most man-made and biological objects exhibit some extent of symmetry. Consider, for example, man-made objects, such as airplanes and houses, or nature-made objects, like fish and insects. Thus, symmetry is an effective cue for visual recognition. This approach is supported by experimental analysis of perceptual grouping and attention in the human visual system [1].

The two most common types of symmetries are rotational and reflectional. An object is said to have rotational symmetry of order N if it is invariant under rotations of $(2\pi/N)n$, $n = 0 \ldots N-1$. An object is said to have reflectional symmetry if it is invariant under a reflection transformation about some line. Hence, symmetry (of both kinds) is an angular property, and as images are given on Cartesian grids, the polar nature of the problem poses computational difficulties.

The algorithm presented in this paper uses the pseudopolar Fourier transform (PPFT) [2] to analyze the angular properties of images in the Fourier domain. This approach has several advantages. First, a polar fast Fourier transform (FFT) is used to generate a polar representation of the image in an algebraically accurate way. Second, by analyzing the magnitude of the polar FFT, we avoid the need to compute the center of rotation, as the magnitude of the FFT is invariant to translations and commutative to rotations. Third, we reformulate the problem of estimating the order of symmetry as the analysis of a periodic one-dimensional (1-D) signal embedded in noise. This is a well-known problem in signal processing with well-tested algorithmic solutions.

The paper is organized as follows. Section II presents previous works related to symmetry detection. Section III provides a mathematical presentation of symmetries as well as the angular properties of the Fourier domain. Section IV presents the angular correlation (AC) as a tool for analyzing symmetries, while discretization and implementation issues are discussed in Section V. Finally, Sections VI and VII present experimental results and concluding remarks, respectively.

II. Previous Work

Symmetry is thoroughly studied in the literature from theoretical, algorithmic, and applicative perspectives. Theoretical treatment of symmetry can be found in [9] and [17]. The algorithmic approaches to symmetry detection can be divided into several categories based on their characteristics. The first characteristic of a symmetry detection algorithm is whether it considers symmetry as a binary or continuous feature, which measures the amount of symmetry. A second characteristic is the type of symmetry detected by the algorithm. Most algorithms detect either rotational or reflectional symmetry, but not both. A third characteristic is the assumptions that are made on the image. For example, whether the algorithm assumes that the image is symmetric or detects it, or whether the algorithm assumes that the symmetry center is located at the center of the image. A fourth characteristic is whether the algorithm operates in the image domain or transforms the problem into a different domain, such as the Fourier domain. A fifth characteristic is the robustness of the algorithm to noise and its ability to operate on real-life nonsynthetic images.

We start by describing local symmetry measures. A low-level, context-free operator for detecting points of interest within an image, which relies on the assumption that context free attention is directed by symmetry, is presented in [13]. The suggested symmetry operator constructs the symmetry map of the image by assigning a symmetry magnitude and symmetry orientation to each pixel. This map is an edge map where the magnitude and orientation of each edge depend on the symmetry associated with each of its pixels. The proposed operator allows one to process different symmetry scales, enabling it to be used in multiresolution schemes. The proposed operator is demonstrated to be effective in detecting points of interest in natural images.

An algorithm for detecting areas with high local reflectional symmetry that is based on a local symmetry operator is presented in [6]. It defines a two-dimensional (2-D) reflectional symmetry measure as a function of four parameters x, y, θ, and r, where x and y are the center of the examined area, r is its

Manuscript received January 30, 2005; revised August 23, 2005. This work was supported by a Grant from the Ministry of Science, Israel. The associate editor coordinating the review of this manuscript and approving it for publication was Dr. Ivan W. Selesnick.

The authors are with theDepartment of Mathematics, Yale Universtiy, New Haven, CT 06520 USA.

Digital Object Identifier 10.1109/TIP.2006.875227

radius, and θ is the angle of the reflection axis. Examining all possible values of x, y, r, and θ is computationally prohibitive; therefore, the algorithm formulates the problem as a global optimization problem and uses a probabilistic genetic algorithm to find the optimal solution efficiently.

As noted previously, symmetry can be considered either as a binary or as a continuous feature. A symmetry distance, which measures the amount of symmetry in an object, is presented in [18]. For an object, given by a sequence of points, the symmetry distance is defined as the minimum distance in which we need to move the points of the original object in order to obtain a symmetric object. This also defines the symmetry transform of an object as the symmetric object that is closest to the given one. Algorithms that compute the symmetry transform of an object with respect to rotational and reflectional symmetries and handle the problem of selecting points to represent 2-D objects are described in [18]. These algorithms require finding point correspondences, which is generally difficult, and perform an exhaustive search over all potential symmetry axes, which is computationally expensive.

Pattern-analysis approaches to symmetry detection define a pixelwise feature vector, which encodes the geometrical structure around each pixel and acts as a local symmetry measure. Then, pixels with similar symmetry measures are clustered together. Such a scheme that detects local, global, and skewed symmetries is described by [15], where an affine invariant feature vector is computed over a set of interest points. Another pattern-analysis approach is introduced in [11], where the feature vector field is based on the location, orientation, and magnitude of the edge gradients. Local features in the form of Taylor coefficients of the field are computed and a hashing algorithm is then applied to detect pairs of points with symmetric fields. A voting scheme is used to robustly identify the location of the symmetry axes.

The works of [4] and [8] are of particular relevance to our approach, as these schemes operate in the Fourier domain, are able to efficiently detect large symmetric objects, and are considered state of the art; [4] analyzes the symmetries of real objects by computing the analytic Fourier–Mellin transform (AFMT). The input image is interpolated on a polar grid in the spatial domain before computing the FFT, resulting in a polar Fourier representation. Yet, this approach comes at the cost of losing the shift invariance of the Fourier magnitudes and, thus, can only be applied to images with known symmetry centers. [8] provides an elegant approach to analyzing the angular properties of an image, without computing its polar discrete Fourier transform (DFT). An angular histogram is computed by detecting and binning the pointwise zero crossings of the difference of the Fourier magnitude in Cartesian coordinates along rays. The histogram's maximum corresponds to the direction of the zero crossing. For real images, most of the zero crossings detected in the Fourier domain are spurious and the binning operation might result in erroneous maximum.

Our approach differs from the above-mentioned schemes in two attributes. First, it uses the PPFT to compute an accurate, translation-invariant polar Fourier representation of the input image. Second, it uses the MUSIC [10] scheme to robustly estimate the order of symmetry. Using the polar representation we define the AC, which measures the correlation between images in the angular direction. We rigorously show that the AC of a symmetric image is a periodic signal whose number of periods corresponds to the order of symmetry. For real images, even the AC computed by our scheme (which is algebraically accurate) is noisy, due to nonperfect symmetries and the nonsymmetric backgrounds (note the Pentagon example in Section V). Hence, we employ a robust, state-of-the-art spectrum estimation technique that enables to analyze real images without preprocessing. Our scheme can also be used to detect multiple symmetric objects within the analyzed image (similar to local methods [6], [5], and [15]), by dividing the input image to sub-images and processing each of them separately.

In terms of pattern analysis, our scheme assumes the existence of a global periodic pattern which is best detected by spectral methods (spectrum estimation). This occurs in images containing large symmetric objects, where we are able to robustly identify high-order symmetries. In contrast, local pattern-analysis schemes [11], [15] are better at detecting cluttered, small symmetric objects, which do not correspond to global periodic patterns.

III. Mathematical Preliminaries

A. Types of Symmetries

Definition (Rotational Symmetry): A function $\psi : \mathbb{R}^2 \to \mathbb{R}$ is rotationally symmetric of order N around the origin if

$$\psi(x, y) = \psi(R_{\beta_n}(x, y)) \tag{III.1}$$

where $\beta_n = (2\pi)/(N)n$, $n = 0, \ldots, N-1$, and $R_{\beta_n} : \mathbb{R}^2 \to \mathbb{R}^2$ is a rotation transformation given by

$$R_{\beta_n}(x, y) = \begin{pmatrix} \cos\beta_n & -\sin\beta_n \\ \sin\beta_n & \cos\beta_n \end{pmatrix} \begin{pmatrix} x \\ y \end{pmatrix}. \tag{III.2}$$

In operator notation, (III.1) is written as $\psi = \psi \circ R_{\beta_n}$, while in polar coordinates, it is given by

$$\psi(r, \theta) = \psi(r, \theta + \beta_n) \tag{III.3}$$

where $\beta_n = \frac{2\pi}{N} n$, $n = 0, \ldots, N-1$.

Definition III.2 (Reflectional Symmetry): A function $\psi : \mathbb{R}^2 \to \mathbb{R}$ is reflectionally symmetric with respect to the vector $(\cos\alpha_0, \sin\alpha_0)$ if

$$\psi(x, y) = \psi(S_{\alpha_0}(x, y)) \tag{III.4}$$

where

$$S_{\alpha_0}(x, y) = \begin{pmatrix} \cos 2\alpha_0 & \sin 2\alpha_0 \\ \sin 2\alpha_0 & -\cos 2\alpha_0 \end{pmatrix} \begin{pmatrix} x \\ y \end{pmatrix}. \tag{III.5}$$

α_0 is the tilt angle of the reflection axis of ψ. An image ψ has reflectional symmetry of order N if there are N angles α_n that satisfy (III.4).

In polar coordinates (III.4) is written as

$$\psi(r, \alpha_0 + \theta) = \psi(r, \alpha_0 - \theta) \tag{III.6}$$

where α_0 is the angle of the reflection axis. If an image ψ has rotational symmetry of order N, then it either has reflectional symmetry of order N or has no reflectional symmetry at all [14], [17]. If an image has both rotational and reflectional symmetry, then the axes of reflectional symmetry are given by

$$\alpha_n = \alpha_0 + \frac{1}{2}\beta_n, \qquad n = 0, \ldots, N-1 \tag{III.7}$$

where α_0 is the angle of one of the reflection axes, and β_n are the angles of rotational symmetry.

A function ψ is rotationally symmetric with center (x_0, y_0), if $\psi(x - x_0, y - y_0)$ is rotationally symmetric around the origin. Similarly, ψ is reflectionally symmetric with respect to a vector $(\cos\alpha_0, \sin\alpha_0)$ that passes through (x_0, y_0) if $\psi(x - x_0, y - y_0)$ is reflectionally symmetric with respect to the vector $(\cos\alpha_0, \sin\alpha_0)$ as given by Definition III.2.

B. Properties of the Fourier Transform

The Fourier transform is the main tool in deriving and analyzing the proposed scheme. In this section we present the definition of the Fourier transform as well as some of its properties that are required for the derivation of the algorithm.

Let $f : \mathbb{R}^2 \to \mathbb{C}$ be a function whose modulus is square integrable on $\mathbb{R}^2$. The 2-D Fourier transform of f, denoted $\hat{f}(\omega_x, \omega_y)$ or $\mathcal{F}(f)(\omega_x, \omega_y)$, is given by

$$\hat{f}(\omega_x, \omega_y) = \int\int_{-\infty}^{\infty} f(x, y) e^{-i(x\omega_x + y\omega_y)}\, dx\, dy \tag{III.8}$$

where $\omega_x, \omega_y \in \mathbb{R}$.

The following lemmas are well known and stated without proofs.

Lemma III.3: If ψ is rotationally symmetric around the origin with order N, then $\hat{\psi}$ is also rotationally symmetric around the origin with the same order. Explicitly

$$\mathcal{F}(\psi) = \mathcal{F}(\psi) \circ R_{\beta_n}, \quad n = 0, \ldots, N-1. \tag{III.9}$$

Lemma III.4: If ψ is reflectionally symmetric with respect to the vector $(\cos\alpha_0, \sin\alpha_0)$, then $\hat{\psi}$ is also reflectionally symmetric with respect to the same vector. Explicitly

$$\mathcal{F}(\psi) = \mathcal{F}(\psi) \circ S_{\alpha_0}. \tag{III.10}$$

C. Pseudopolar Fourier Transform

Given an image I of size $N \times N$, its 2-D Fourier transform, denoted as $\widehat{I}(\omega_x, \omega_y)$, is given by

$$\widehat{I}(\omega_x, \omega_y) = \sum_{u,v=-N/2}^{N/2-1} I(u, v) e^{-i(u\omega_x + v\omega_y)} \qquad \omega_x, \omega_y \in \mathbb{R}. \tag{III.11}$$

We assume for simplicity that the image I has equal dimensions in the x and y directions and that N is even. If ω_x and ω_y are sampled on the Cartesian grid $(\omega_x, \omega_y) = (2\pi)/(M)(k, l), k, l = -M/2, \ldots, M/2 - 1, M = 2N + 1$, then (III.11) has the form

$$\widehat{I}(k, l) \triangleq \sum_{u,v=-N/2}^{N/2-1} I(u, v) e^{-\frac{2\pi i}{M}(uk + vl)} \tag{III.12}$$

$k, l = -(M/2), \ldots, (M/2) - 1$, which is usually referred to as the 2-D DFT of the image I. The parameter M $(M > N)$ sets the frequency resolution of the DFT. It is well known that the DFT of I, given by (III.12), can be computed with algorithms having complexity $O(M^2 \log M)$.

For some applications, it is desirable to compute the Fourier transform of I on a polar grid. Formally, we want to sample the Fourier transform in (III.11) on the grid

$$\begin{aligned} &\omega_x = r_k \cos\theta_l, \quad \omega_y = r_k \sin\theta_l \\ &r_k = \frac{2\pi k}{M}, \quad \theta_l = 2\pi l / L \\ &k = 0, \ldots, M-1, \quad l = 0, \ldots, L-1 \end{aligned} \tag{III.13}$$

for which the Fourier transform in (III.11) has the form

$$\widehat{I}_{\text{polar}}(k, l) \triangleq \widehat{I}(r_k \cos\theta_l, r_k \sin\theta_l). \tag{III.14}$$

The grid given by (III.13) is equally spaced both in the radial and angular directions

$$\Delta r_p(k) \triangleq r_{k+1} - r_k = \frac{2\pi}{M} \tag{III.15}$$

$$\Delta\theta_p(l) \triangleq \theta_{l+1} - \theta_l = \frac{2\pi}{L}. \tag{III.16}$$

The PPFT defined below produces nonuniform polar samples of $\widehat{I}$. It is accurate and can be computed using a fast algorithm. Thus, for practical implementations, we use the pseudopolar grid instead of the polar one.

The PPFT evaluates the 2-D Fourier transform of an image on the pseudopolar grid, which approximates the polar grid. Formally, the pseudopolar grid is given by the set of samples

$$P \triangleq P_1 \cup P_2 \tag{III.17}$$

where

$$P_1 \triangleq \left\{ \frac{2\pi}{M}\left(-\frac{2l}{N}k, k\right) \,\middle|\, -\frac{N}{2} \le l \le \frac{N}{2},\ -N \le k \le N \right\} \tag{III.18}$$

$$P_2 \triangleq \left\{ \frac{2\pi}{M}\left(k, -\frac{2l}{N}k\right) \,\middle|\, -\frac{N}{2} \le l \le \frac{N}{2},\ -N \le k \le N \right\}. \tag{III.19}$$

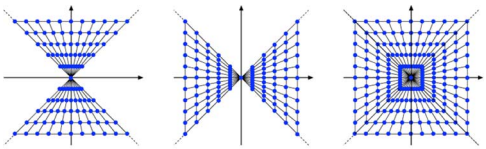

Fig. 1. Pseudopolar grid. (a) and (b) are the pseudopolar sectors P_1 and P_2, respectively. (c) The pseudopolar grid $P = P_1 \cup P_2$. (a) The pseudopolar sector P_1. (b) The pseudopolar sector P_2. (c) The pseudopolar grid. (Color version available online at http://ieeexplore.ieee.org.)

The pseudopolar grid P is illustrated in Fig. 1(c). As can be seen from Fig. 1(a) and (b), k serves as a "pseudoradius" and l serves as a "pseudoangle." The resolution of the pseudopolar grid is $N+1$ in the angular direction and $M = 2N+1$ in the radial direction. Using a polar coordinate representation, the pseudopolar grid is given by

$$P_1(k,l) = \left(r_k^1, \theta_l^1\right), \quad P_2(k,l) = \left(r_k^2, \theta_l^2\right) \tag{III.20}$$

$$r_k^1 = r_k^2 = \frac{2\pi k}{M}\sqrt{4\left(\frac{l}{N}\right)^2 + 1} \tag{III.21}$$

$$\theta_l^1 = \pi/2 - \arctan\left(\frac{2l}{N}\right), \quad \theta_l^2 = \arctan\left(\frac{2l}{N}\right) \tag{III.22}$$

where $k = -N, \ldots, N$ and $l = -N/2, \ldots, N/2$. We define the PPFT as the samples of the Fourier transform $\widehat{I}$, given in (III.11), on the pseudopolar grid P, given by (III.17). Formally, the PPFT $\widehat{I}_{\mathrm{PP}}^j$ $(j = 1, 2)$ is a linear transformation, which is defined for $k = -N, \ldots, N$ and $l = -N/2, \ldots, N/2$, as

$$\widehat{I}_{\mathrm{PP}}^1(k,l) \triangleq \widehat{I}\left(\frac{2\pi}{M}\left(-\frac{2l}{N}k, k\right)\right) \tag{III.23}$$

$$\widehat{I}_{\mathrm{PP}}^2(k,l) \triangleq \widehat{I}\left(\frac{2\pi}{M}\left(k, -\frac{2l}{N}k\right)\right) \tag{III.24}$$

where $\widehat{I}$ is given by (III.11).

As we can see in Fig. 1(c), for each fixed angle l, the samples of the pseudopolar grid are equally spaced in the radial direction. However, this spacing is different for different angles. Also, the grid is not equally spaced in the angular direction, but has equally spaced slopes. Formally

$$\Delta \tan \theta_{pp}^1(l) \triangleq \cot \theta_{l+1}^1 - \cot \theta_l^1 = \frac{2}{N} \tag{III.25}$$

$$\Delta \tan \theta_{pp}^2(l) \triangleq \tan \theta_{l+1}^2 - \tan \theta_l^2 = \frac{2}{N} \tag{III.26}$$

where θ_l^1 and θ_l^2 are given in (III.22) Two important properties of the PPFT are that it is invertible and that both the forward and inverse PPFTs can be implemented using fast algorithms. Moreover, their implementations require only the application of 1-D equispaced FFTs. In particular, the algorithms do not require re-gridding or interpolation.

The algorithm for computing the PPFT is based on the fractional Fourier transform (FRFT). The FRFT [16], with its generalization given by the Chirp Z-transform [12], is a fast $O(N \log N)$ algorithm that evaluates the Fourier transform of a sequence X on any set of N equally spaced points on the unit circle. By using the FRFT we compute the PPFT $\widehat{I}_{\mathrm{PP}}^1$, given in (III.23), as follows.

Algorithm 1 Computing the pseudopolar Fourier transform

1: Zero pad the image I to size $N \times (2N+1)$ (along the y direction).

2: Apply the 1-D Fourier transform to each column of I (along the y direction).

3: Apply the FRFT to each row (in the x direction) with $\alpha = 2k/n$, where k is the index of the row.

The algorithm that computes $\widehat{I}_{\mathrm{PP}}^2$ is similar. The complexity of computing $\widehat{I}_{\mathrm{PP}}^1$ of an $N \times N$ image is $O(N^2 \log N)$. Since the complexity of computing $\widehat{I}_{\mathrm{PP}}^2$ is also $O(N^2 \log N)$, the total complexity of computing the PPFT is $O(N^2 \log N)$.

IV. Continuous Formulation

A. Computing the Order of Symmetry of Centered Symmetries

For a function $\psi : \mathbb{R}^2 \to \mathbb{R}$, given in polar coordinates, we define its expectation with respect to r over the interval $[0, r_0]$ as

$$\langle \psi \rangle = \frac{1}{r_0}\int_0^{r_0} \psi(r,\theta)\,\frac{dr}{r}.$$

Due to numerical problems arising in its computation, according to [3], we use the following expression:

$$\langle \psi \rangle = \frac{1}{r_0}\int_0^{r_0} r^\nu \psi(r,\theta)\,\frac{dr}{r} \tag{IV.1}$$

with $\nu = 1$. We define the standard deviation of ψ with respect to r as

$$\sigma(\psi) = \sqrt{\langle \psi^2 \rangle - \langle \psi \rangle^2}. \tag{IV.2}$$

Definition IV.1: Let $\psi : \mathbb{R}^2 \to \mathbb{R}$. The AC, denoted $g_\psi(\theta)$, of $\psi(r,\theta)$ and $\psi(r,-\theta)$ is given by

$$g_\psi(\theta) = \frac{\langle \psi(r,\theta)\psi(r,-\theta)\rangle - \langle \psi(r,\theta)\rangle\langle \psi(r,-\theta)\rangle}{\sigma(\psi(r,\theta))\,\sigma(\psi(r,-\theta))}. \tag{IV.3}$$

From the definition, $-1 \le g_\psi(\theta) \le 1$. It is clear that if ψ is rotationally symmetric of order N (Definition III.1), then $\langle \psi \rangle$ and $\sigma(\psi)$ are periodic with N periods over $[0, 2\pi)$. An example of the AC of a symmetric image is given in Fig. 2.

Lemma IV.2: If ψ is rotationally symmetric of order N, as given by Definition III.1, then $g_\psi(\theta)$, given by (IV.3), is periodic with period $\beta_1 = 2\pi/N$. Moreover, $g_\psi(\beta_n) = 1, n = 0, \ldots, N-1$.

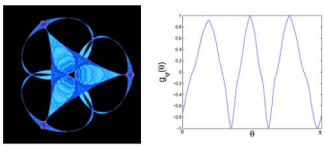

(a) (b)

Fig. 2. AC function $g_\psi(\theta)$ of a symmetric image. $g_\psi(\theta)$ contains three periods corresponding to the order of rotational symmetry in (a). (Color version available online at http://ieeexplore.ieee.org.)

Proof: From (III.3) and the fact that $\beta_n = (2\pi)/(N)n$ we get for $n = 0, \ldots, N-1$

$$\begin{aligned} g_\psi(\theta+\beta_n) &= \frac{\langle \psi(r,\theta+\beta_n)\psi(r,-(\theta+\beta_n))\rangle}{\sigma(\psi(r,\theta+\beta_n))\sigma(\psi(r,-(\theta+\beta_n)))} \\ &\quad - \frac{\langle \psi(r,\theta+\beta_n)\rangle\langle \psi(r,-(\theta+\beta_n))\rangle}{\sigma(\psi(r,\theta+\beta_n))\sigma(\psi(r,-(\theta+\beta_n)))} \\ &= \frac{\langle \psi(r,\theta)\psi(r,-\theta)\rangle - \langle \psi(r,\theta)\rangle\langle \psi(r,-\theta)\rangle}{\sigma(\psi(r,\theta))\sigma(\psi(r,-\theta))} \\ &= g_\psi(\theta). \end{aligned}$$

Since $g_\psi(0) = 1$ and $g_\psi(\theta)$ is periodic, it is clear that $g_\psi(\beta_n) = 1, n = 0, \ldots, N-1$. ■

Lemma IV.2 suggests that it is possible to compute the order of symmetry of ψ by finding the number of periods of $g_\psi(\theta)$ in $[0, 2\pi]$. The symmetry axes for reflectional symmetry are then given by

$$\alpha_n = \alpha_0 + \frac{1}{2}\beta_n, \quad n = 0, \ldots, N-1$$

where α_0 is the tilt angle of one of the axes.

B. Finding the Tilt Angle of a Reflection Axis

The following lemma shows how to compute α_0 by relating it to the registration of two images.

Lemma IV.3: The tilt angle of one of the reflection axes of an image $\psi(r,\theta)$, denoted α_0, can be computed by registering $\psi(r,\theta)$ to $\psi(r,-\theta)$.

Proof: By (III.6), we have

$$\begin{aligned} \psi(r,-\theta) &= \psi(r,\alpha_0+(-\theta-\alpha_0)) = \psi(r,\alpha_0-(-\theta-\alpha_0)) \\ &= \psi(r,2\alpha_0+\theta). \end{aligned}$$

Hence, $\psi(r,\theta)$ and $\psi(r,-\theta)$ are related by a rotation angle of $2\alpha_0$. ■

Lemma IV.3 is exemplified by Fig. 3. Next, we show that rotated images can be registered by a variant of the AC given in Definition IV.1.

Lemma IV.4: Let $\psi_1 : \mathbb{R}^2 \to \mathbb{R}, \psi_2 : \mathbb{R}^2 \to \mathbb{R}$, and define

$$g_{\psi_1,\psi_2}(\theta) = \frac{\langle \psi_1(r,\theta)\psi_2(r,-\theta)\rangle - \langle \psi_1(r,\theta)\rangle\langle \psi_2(r,-\theta)\rangle}{\sigma(\psi_1(r,\theta))\,\sigma(\psi_2(r,-\theta))}. \quad \text{(IV.4)}$$

If ψ_2 is a rotated replica of ψ_1, that is $\psi_2(r,\theta) = \psi_1(r,\theta+\Delta\theta)$, then $g_{\psi_1,\psi_2}(\Delta\theta/2) = 1$.

Proof: Since $\psi_2(r,\theta) = \psi_1(r,\theta+\Delta\theta)$, we have that $\psi_2(r,-\theta) = \psi_1(r,-\theta+\Delta\theta)$. Substituting into (IV.4), we get (IV.5), shown at the bottom of the page, and $g_{\psi_1,\psi_2}(\Delta\theta/2) = 1$. ■

Next, we apply Lemma IV.4 to the particular problem of recovering the symmetry axis' angle.

Theorem IV.5: Given a reflectionally symmetric image $\psi(r,\theta)$, the angle of its reflection axis, denoted α_0, can be estimated from $g_{\psi_1,\psi_2}(\theta)$ with $\psi_1(r,\theta) = \psi(r,\theta)$ and $\psi_2(r,\theta) = \psi(r,-\theta)$. In this case, $g_{\psi_1,\psi_2}(\theta)$ is denoted as $g_{\psi^+,\psi^-}(\theta)$.

Proof: Let $\psi_1(r,\theta) = \psi(r,\theta)$ and $\psi_2(r,\theta) = \psi(r,-\theta)$. Using Lemma IV.3 , ψ_1 and ψ_2 are related by a rotation of $2\alpha_0$. This angle is recovered by applying the registration scheme suggested in Lemma IV.4; moreover, $g_{\psi^+,\psi^-}(\alpha_0) = 1$. ■

The application of Theorem IV.5 to the magnitudes of the Fourier transforms of the images to register allows to recover α_0 regardless of the relative translation between the images.

Theorem IV.6: The AC between the magnitudes of the Fourier transforms of the images to register shows two maxima over $[0,\pi]$. The maxima are $\frac{\pi}{2}$ apart and can be mapped into the interval $[0,\pi/2]$. The implementation requires the rotation of the input images by an arbitrary predefined angle γ.

Proof: From the conjugate symmetry of the Fourier transform, we get $|\widehat{\psi}(r,\theta)| = |\widehat{\psi}(r,\theta+\pi)|$. Hence, the equation $g_{|\widehat{\psi}|^+,|\widehat{\psi}|^-}(\theta) = 1$ (IV.5) has at least two solutions. The first solution is $\theta_0 = \Delta\theta/2$, where $\Delta\theta$ is the relative rotation between the images. The second, which results from the conjugate symmetry $|\hat{\psi}(r,\theta_0)| = |\hat{\psi}(r,-\theta_0+\Delta\theta+\pi)|$, is $\theta_1 = \Delta\theta/2+\pi/2$. We combine the two solutions to improve the robustness and accuracy of the estimation by defining

$$\widetilde{g}_{\psi^+,\psi^-}(\theta) \triangleq g_{|\widehat{\psi}|^+,|\widehat{\psi}|^-}(\theta) + g_{|\widehat{\psi}|^+,|\widehat{\psi}|^-}\left(\theta+\frac{\pi}{2}\right) \quad \text{(IV.6)}$$

and computing

$$\theta_0 = \arg\max_{\theta\in[0,\pi/2]} \{\widetilde{g}_{|\widehat{\psi}|^+,|\widehat{\psi}|^-}(\theta)\}.$$

$$g_{\psi_1,\psi_2}(\theta) = \frac{\langle \psi_1(r,\theta)\psi_1(r,-\theta+\Delta\theta)\rangle - \langle \psi_1(r,\theta)\rangle\langle \psi_1(r,-\theta+\Delta\theta)\rangle}{\sigma(\psi_1(r,\theta))\,\sigma(\psi_1(r,-\theta+\Delta\theta))} \quad \text{(IV.5)}$$

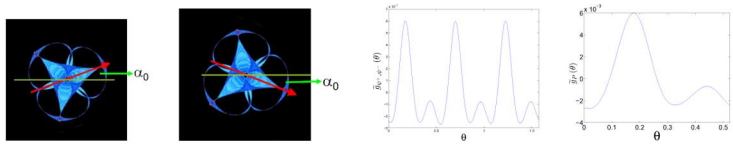

Fig. 3. Recovering the tilt angle of one of the reflection axes. (a) The image has a reflectional symmetry axis tilted by α_0. (b) The image is flipped upside down and the axis is tilted by an angle $-\alpha_0$. Note that there are three equivalent solutions for the registration of (b) to (a). (c) The reflectional AC $\widetilde{g}_{\psi^+,\psi^-}(\theta)$ computed by (a) and (b). The three maxima corresponding to the three solutions are evident. (d) Folding the three periods gives the basic interval $\widetilde{g}_P(\theta)$, whose maximum corresponds to the angle α_0. (Color version available online at http://ieeexplore.ieee.org.)

For reflectionally symmetric images, $\psi(r,\alpha_0+\theta) = \psi(r,\alpha_0-\theta)$. Thus, if $\alpha_0=0$ and $\psi(r,\alpha_0-\theta)$ is computed by flipping ψ upside down, then

$$\psi_1(r,\theta)=\psi(r,\theta)=\psi(r,-\theta)=\psi_2(r,\theta)$$

and $g_{|\widehat{\psi}|^+,|\widehat{\psi}|^-}(\theta)=1$ for every θ. This means that, in this case, it is impossible to recover $\Delta\theta$ from $g_{|\widehat{\psi}|^+,|\widehat{\psi}|^-}(\theta)$. Hence, the image has to be flipped around an axis which is not a symmetry axis, and so instead of registering $\widehat{\psi}(r,\theta)$ to $\widehat{\psi}(r,-\theta)$, we register $\widehat{\psi}(r,\theta)$ to $\widehat{\psi}(r,-\theta+\gamma)$, where γ is an arbitrary chosen angle. ■

Hence, α_0 can be recovered by registering $\psi(r,\theta)$ to $\psi(r,-\theta)$ using the AC, where $\psi(r,-\theta)$ is computed by flipping $\psi(r,\theta)$ upside down. The robustness is improved by utilizing our knowledge of the order of symmetry N. The registration problem in Theorem IV.5 has N solutions (see Fig. 3), and, thus, $\widetilde{g}_{\psi^+,\psi^-}(\theta)$ has N periods over $[0,\pi/2]$, that is

$$\widetilde{g}_{\psi^+,\psi^-}(\alpha_0)=\widetilde{g}_{\psi^+,\psi^-}\left(\alpha_0+\frac{\pi}{2N}n\right),\quad n=0,\ldots,N-1.$$

We denote by $\widetilde{g}_{\psi^+,\psi^-}(\alpha_0)$ the reflectional AC, as it measures the AC of an image with its reflected replica.

Similar to (IV.6), we utilize the periodicity by folding $\widetilde{g}_{\psi^+,\psi^-}(\theta)$ from $[0,\pi/2]$ to $[0,(\pi)/(2N)]$

$$\widetilde{g}_P(\theta)=\sum_{k=0}^{N-1}\widetilde{g}_{\psi^+,\psi^-}\left(\theta+k\frac{\pi}{2N}\right) \tag{IV.7}$$

and looking for

$$\theta_0=\arg\max_{\theta\in[0,\frac{\pi}{2N}]}\{\widetilde{g}_P(\theta)\}.$$

Due to the conjugate symmetry mentioned above, both θ_0 and $\theta_0+\frac{\pi}{2}$ are possible solutions, corresponding to rotations of $2\theta_0$ and $2\theta_0+\pi$, respectively. If N is even, either of them can be used, as both α_0 and $\alpha_0+(\pi/2)$ are valid tilt angles of a symmetry axis. If N is odd, the ambiguity is resolved by rotating the image according to both angles ($2\theta_0$ and $2\theta_0+\pi$), computing the phase correlation [7], and choosing the one with the highest correlation peak. Finally, by Theorem IV.6 we have that $\theta_0=(\Delta\theta)/(2)=(1/2)(2\alpha_0+\gamma)$ and α_0 is given by

$$\alpha_0=\theta_0-\frac{\gamma}{2}. \tag{IV.8}$$

As any image can be registered to its rotated replica, we get $N=1$ both for nonsymmetric images and for images with a single reflectional symmetry axis. Thus, we analyze $\widetilde{g}_{\psi^+,\psi^-}(\theta)$ to see whether it has a dominant maximum. Consider, for example, Figs. 5 and 7: In both cases, the function $g_\psi(\theta)$ has a single period and the difference being the number of periods, as $\widetilde{g}_{\psi^+,\psi^-}(\theta)$, has no periods in Fig. 7 compared to one in Fig. 5.

C. Computing the Order of Symmetry of Noncentered Symmetries

In this section, we extend the approach suggested in Section IV-A to handle noncentered symmetries. By using Lemmas III.3 and III.4, and the translation invariance of the Fourier transform's magnitude, we obtain Lemma IV.7, which enables to convert noncentered symmetric functions into functions that are symmetric around the origin.

Lemma IV.7: Let ψ_1 be a rotationally symmetric function of order N around (x_0,y_0). Then, $|\hat{\psi}_1|^2$, where $\hat{\psi}_1$ is the 2-D Fourier transform of ψ_1, is rotationally symmetric of order N around the origin.

Lemma IV.7 suggests the processing of noncentered symmetries by applying the algorithm from Section IV.A to the magnitude of the Fourier transform of the input function. This gives the order of symmetry N and the reflection axes $\alpha_n, n=0,\ldots,N-1$. Therefore, the analog of $g_\psi(\theta)$ (IV.3) for noncentered functions is defined as

$$E_\psi(\theta)=\frac{\langle|\hat{\psi}(r,\theta)|^2|\hat{\psi}(r,-\theta)|^2\rangle-\langle|\hat{\psi}(r,\theta)|^2\rangle\langle|\hat{\psi}(r,-\theta)|^2\rangle}{\sigma(|\hat{\psi}(r,\theta)|^2)\,\sigma(|\hat{\psi}(r,-\theta)|^2)} \tag{IV.9}$$

and the algorithm of Section IV.A is applied to $E_\psi(\theta)$.

As ψ_1 is real, $\hat{\psi}_1$ is conjugate symmetric $|\hat{\psi}_1(r,\theta)| = |\hat{\psi}_1(r,\theta+\pi)|$. Thus, N symmetry axes in $|\hat{\psi}_1|^2$ can result from either N or $2N$ symmetry axes in ψ_1. This ambiguity is resolved by rotating ψ_1 by both $\theta_1 = (2\pi)/(N)$ and $\theta_2=(2\pi)/(2N)=(\pi/N)$ and comparing the phase correlation peaks [7]. Note that θ_1 is necessarily a valid solution for the rotation for both N and $2N$ symmetry axes.

D. Computing the Center of Symmetry

After computing the order of symmetry N, we recover the center of symmetry $C=(x_0,y_0)$. Our approach is based on the observation that a symmetric image ψ and its replica, rotated

by $(2\pi)/(N)$, are related by a pure translation. This translation maps C to itself.

This applies to both reflectional and rotational symmetries as a reflectionally symmetric image is also rotationally symmetric [14]. We compute a transformation Q that maps C to itself by rotating ψ by $\theta = (2\pi)/(N)$ (N is already known at this point) and recovering the residual translation T. Q is given by $Q = TR_\theta$ and as C is mapped to itself $QC = C, C$ is the eigenfunction of Q corresponding to the eigenvalue $\lambda = 1$. In practice, Q, T, and R_θ are represented as matrices and C is an eigenvector. This is summarized in Algorithm 2.

Algorithm 2 Computing the center of symmetry

1: Rotate the input image by $\theta = (2\pi)/(N)$ and denote the rotated image as $\widetilde{\psi}$.

2: Compute the corresponding rotation matrix R_θ.

3: Recover the translation T between ψ and $\widetilde{\psi}$ using phase correlation [7].

4: Compute $Q = TR_\theta$.

5: C is an eigenvector of Q corresponding to the eigenvalue $\lambda = 1$.

V. Scheme Discretization

Discretizing the approach suggested in Section IV poses several difficulties.

1) The continuous formulation is based on a polar representation of the Fourier transform of the input function. In order to use this approach in discrete settings, we need a fast and accurate way to generate a polar representation of the Fourier transform of a discrete image.
2) The formulation of $E_\psi(\theta)$ in (IV.9) uses continuous definitions of expectation and standard deviation, which need to be discretized.

We define a discrete polar representation of the continuous Fourier transform $\hat{\psi}$ as

$$\widehat{\Psi} = \{\hat{\psi}(r\cos\theta, r\sin\theta) \,|\, (r,\theta) \in \Gamma\}$$

and choose the grid Γ to be the pseudopolar grid, for which we have an efficient numerical scheme. To define a discrete version of (IV.9), we define the discrete expectation as

$$\langle\widehat{\Psi}\rangle = \frac{1}{N(r)} \sum_{\substack{(r,\cdot)\in\Gamma \\ r<\pi}} \widehat{\Psi}(r,\theta) \tag{V.1}$$

where $N(r)$ is the number of samples of the form $(r,\cdot) \in \Gamma$ for a fixed θ, such that $r < \pi$. We define the standard deviation in the discrete case as

$$\sigma(\psi) = \sqrt{\langle\widehat{\Psi}^2\rangle - \langle\widehat{\Psi}\rangle^2}. \tag{V.2}$$

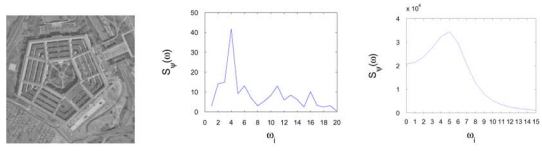

(a) (b) (c)

Fig. 4. Estimating $S_\psi(\omega)$. For real images, such as the *Pentagon* (a), using the FFT to estimate $S_\psi(\omega)$ results in a noisy estimate (b). The MUSIC spectrum estimation scheme gives an accurate result (c).

The notation in the discrete case is the same as in the continuous case. It is clear from the context which definition should be used. In (V.1), we sum over the radial axis, and, therefore, we are interested in discrete polar representations such that for every θ there are roughly the same number of values r such that $(r,\theta) \in \Gamma, r < \pi$. We approximate (IV.9) by

$$\tilde{E}_\psi(\theta) = \frac{\langle|\widehat{\Psi}(r,\theta)|^2|\widehat{\Psi}(r,-\theta)|^2\rangle}{\sigma(|\widehat{\Psi}(r,\theta)|^2)\,\sigma(|\widehat{\Psi}(r,-\theta)|^2)} - \frac{\langle|\widehat{\Psi}(r,\theta)|^2\rangle\langle|\widehat{\Psi}(r,-\theta)|^2\rangle}{\sigma(|\widehat{\Psi}(r,\theta)|^2)\,\sigma(|\widehat{\Psi}(r,-\theta)|^2)} \tag{V.3}$$

where, in practice, $\widehat{\Psi}$ is given by the PPFT of the input image.

In order to estimate the number of periods of $\tilde{E}_\psi(\theta)$, we compute its spectrum, denoted $S_\psi(\omega)$, using nonparametric spectrum estimation [10]. If $\tilde{E}_\psi(\theta)$ has N periods over $[0,\pi]$, then $S_\psi(\omega)$ has a maximum at ω_N. Since $\tilde{E}_\psi(\theta)$ is defined over a nonuniform abscissa of θ, given in (III.22), we resample it on a uniform θ axis. Fig. 4(c) shows the spectrum estimate $S_\psi(\omega)$ of the *Pentagon* image computed by the MUSIC algorithm [10], which estimates the frequency content by an eigenvalue decomposition of the signal's correlation matrix. The MUSIC algorithm is particularly suitable for the analysis of signals that are the sum of sinusoids and additive white Gaussian noise. Approximating $S_\psi(\omega)$ by the magnitude of the FFT results in a wrong estimate of the dominant frequency [Fig. 4(b)].

VI. Experimental Results

The proposed approach was tested using real images with noncentered symmetries. Color images were converted to greyscale before being analyzed. The spectrum $S_\psi(\omega)$ was computed in all cases using a MUSIC algorithm without zero padding. For each image we present $\tilde{E}_\psi(\theta), \widetilde{g}_{\psi^+,\psi^-}(\theta)$ [(V.3) and (IV.6)], the spectrum $S_\psi(\omega)$ used to recover the order of symmetry, and the estimated axes and center of symmetry. For reflectional symmetries, we show $\widetilde{g}_P(\theta)$ (IV.7) and describe the computation of α_0, the angle of one of the symmetry axes, using (IV.8) and $\widetilde{g}_{\psi^+,\psi^-}(\theta)$, where $\gamma = -90°$. In our implementation, we denote $\widehat{\theta}_0 = \arg\min_\theta\{\widetilde{g}_P(\theta)\}$, and the true angle in which that maximum is obtained is $\theta_0 = \widehat{\theta}_0 - 45°$. This is due to the angle ordering in the output array of the PPFT.

As natural objects often exhibit a low order of symmetry, we start by analyzing images containing objects with low order symmetries in Figs. 5 and 6. Both $\tilde{E}_\psi(\theta)$ and $\widetilde{g}_{\psi^+,\psi^-}(\theta)$ contain a single maximum corresponding to $N = 1$, which is detected by the spectrum $S_\psi(\omega)$. Therefore, $\widetilde{g}_P(\theta) = \widetilde{g}_{\psi^+,\psi^-}(\theta)$ and the

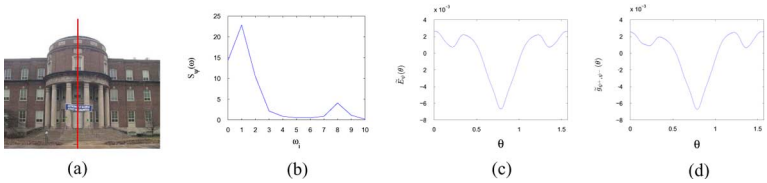

Fig. 5. Reflectional symmetry detection. (a) The symmetry axis is overlaid on the image. (b) The spectrum of the AC where the peak corresponds to a single symmetry axis. (c)The AC $\bar{E}_{\psi}(\theta)$ has a single period. (d) The reflectional AC $\widetilde{g}_{\psi+,\psi-}(\theta)$ used to compute the symmetry axis' angle. (Color version available online at http://ieeexplore.ieee.org.)

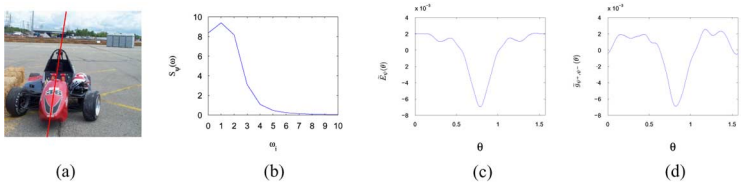

Fig. 6. Reflectional symmetry detection. (a) The symmetry axis is overlaid on the image. (b) The spectrum of the AC. The peak corresponds to a single symmetry axis. (c) The AC $\bar{E}_{\psi}(\theta)$. (d) The reflectional AC $\widetilde{g}_{\psi+,\psi-}(\theta)$ used to compute the angle α_0. (Color version available online at http://ieeexplore.ieee.org.)

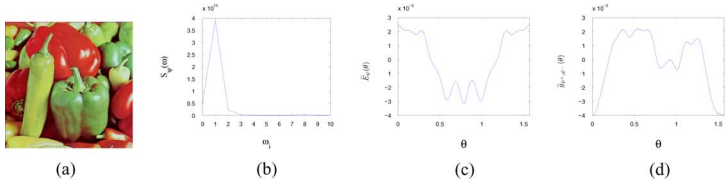

Fig. 7. Analyzing a nonsymmetric image. (a) The "Peppers" image. (b) The spectrum of the AC. The peak corresponds to a single symmetry axis. (c) The AC $\bar{E}_{\psi}(\theta)$ shows the existence of a single registration solution, as an image can always be registered to a rotated replica of itself. Yet, $\widetilde{g}_{\psi+,\psi-}(\theta)$ in (d) does not have a dominant maximum due to the lack of symmetry axes in the image. (Color version available online at http://ieeexplore.ieee.org.)

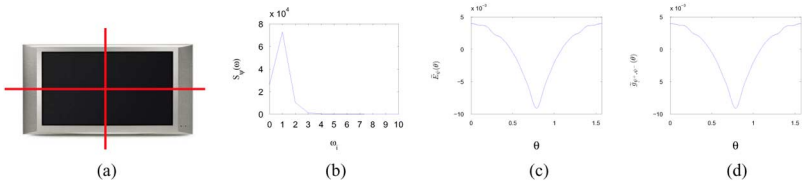

Fig. 8. Reflectional symmetry detection. (a) The symmetry axis is overlaid on the image. (b) The spectrum of the AC. The peak corresponds to a single symmetry axis, and by checking for N and $2N$, we detect two symmetry axes. (c) The AC $\bar{E}_{\psi}(\theta)$. (d) The reflectional AC $\widetilde{g}_{\psi+,\psi-}(\theta)$ used to compute the symmetry axes' angle. (Color version available online at http://ieeexplore.ieee.org.)

maximum of $\widetilde{g}_{\psi+,\psi-}(\theta)$ in Fig. 5(d) is detected at $\widehat{\theta}_0 = 0°$ and $\theta_0 = -45°$. Using (IV.8) we get $\alpha_0 = \theta_0 - (\gamma)/(2) = 0°$ corresponding to the vertical symmetry axis depicted in Fig. 5(a). In Fig. 6(d), $\widehat{\theta}_0 = 9.97°$ and we get $\alpha_0 = \widehat{\theta}_0 - 45° - \frac{\gamma}{2} = 9.97°$. The background in Fig. 6(a) is cluttered and we see that the maximum of $\widetilde{g}_{\psi+,\psi-}(\theta)$ in Fig. 6(d) is less evident than the one in Fig. 5(d).

In contrast, Fig. 7 contains a nonsymmetric image and we get $N = 1$ from $\tilde{E}_{\psi}(\theta)$ and $S_{\psi}(\omega)$. Yet, $\widetilde{g}_{\psi+,\psi-}(\theta)$ does not contain any dominant maximum nor periodic patterns, and, hence, no symmetry axes are detected. This is emphasized by comparing Fig. 7(d) and (c). As we can always register an image to itself, we expect to find a single period of $\tilde{E}_{\psi}(\theta)$ in Fig. 7(c).

The analysis of images with higher orders of symmetry is presented in Figs. 8–10. In Fig. 8, the image and its background are both symmetric and the symmetry axes are easily detected. $\tilde{E}_{\psi}(\theta)$ in Fig. 8(c) contains a single period and from $S_{\psi}(\omega)$ [Fig. 8(b)], we get $N = 1$. Next, we resolve the ambiguity of having either $N = 1$ or $2N = 2$ symmetry axes by rotating the image by $\theta_1 = (2\pi)/(2N) = \pi$ and verifying that it corresponds to a solution of registering the image to itself. Similar to Fig. 5, we get $\alpha_0 = \widehat{\theta}_0 = 0°$.

Fig. 9 is an example of rotational symmetry, which has a symmetry center but no symmetry axes. The spectrum shown in Fig. 9(b) identifies the order of symmetry as $N = 3$, and by rotating the image by both $\theta_1 = (2\pi)/(3)$ and $\theta_2 = (2\pi)/(6)$, we get that the true order of symmetry is $N = 6$. The symmetry center is recovered as described in Section IV-.D. Similar to the results shown in Fig. 7, the periodic pattern is well observed in Fig. 9(c) and less obvious in Fig. 9(d).

Another example is given in Fig. 10, where the object is embedded in clutter. Perceptually, the Pentagon has a clear reflectional symmetry of order five. However, by a close examination of the image, it follows that its symmetry is far from being perfect. This problem is typical of real images and can be effectively addressed by the proposed scheme. Both $\tilde{E}_{\psi}(\theta)$ and $\widetilde{g}_{\psi+,\psi-}(\theta)$ in Fig. 10(c) and (d), respectively, have five periods, which are accurately detected using $S_{\psi}(\omega)$. α_0 is computed

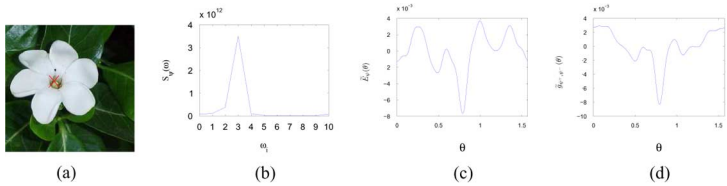

Fig. 9. Rotational symmetry of order 6. (a) The symmetry center is accurately estimated. (b) The maximum of the spectrum corresponds to $N = 3$. By checking for N and $2N$, we detect six symmetry axes. (c) The AC $\bar{E}_\psi(\theta)$ has three periods. (d) The reflectional AC $\widetilde{g}_{\psi+,\psi-}(\theta)$ has no dominant maximum, as the image is not reflectionally symmetric. (Color version available online at http://ieeexplore.ieee.org.)

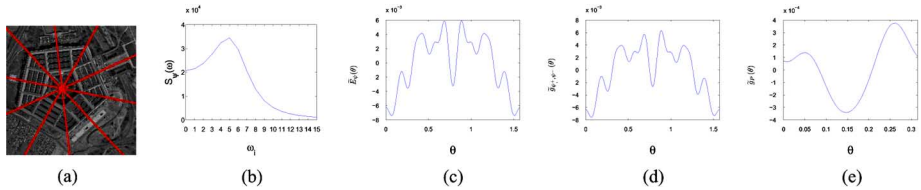

Fig. 10. Detecting reflectional symmetry of order five in a real image with noncentered and nonperfect symmetry. (a) The symmetry axes and center are accurately detected. (b) The maximum of the spectrum corresponds to the number of symmetry axes. (c) The AC $\bar{E}_\psi(\theta)$ has five periods. (d) The reflectional AC $\widetilde{g}_{\psi+,\psi-}(\theta)$ used to compute the symmetry axes' angle also shows five periods. (e) The maximum of $\widetilde{g}_P(\theta)$ corresponds to the tilt angle of one of the symmetry axes. (Color version available online at http://ieeexplore.ieee.org.)

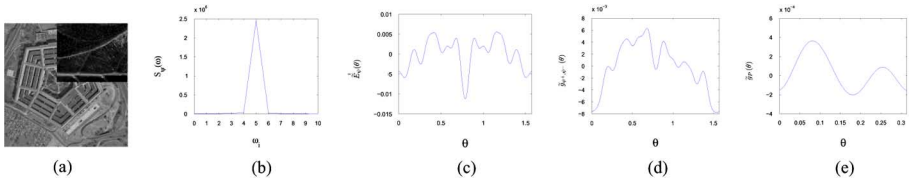

Fig. 11. Detecting reflectional symmetry under occlusion. (a) The Pentagon is occluded by a patch. (b) The maximum of the spectrum corresponds to the number of symmetry axes. (c) The AC $\bar{E}_\psi(\theta)$ has five periods. (d) $\widetilde{g}_{\psi+,\psi-}(\theta)$, used to compute the angle α_0, also shows five periods. (e) $\widetilde{g}_P(\theta)$ differs from the one in Fig. 10(e), causing our scheme to fail to locate the symmetry axes.

using $\widetilde{g}_P(\theta)$, given by (IV.7) and shown in Fig. 10(e), where the maximum is detected at $\widehat{\theta}_0 = 14.89°$ and $\theta_0 = -30.11°$. As N is odd , we verify whether the rotation is either $2\theta_0$ or $2\theta_0 + \pi$ and the true rotation turns to be the latter. Hence, the correct solution in this case is not θ_0 but $\theta_0 + 45° = 59.89°$ and $\alpha_0 = \theta_0 + 45° = 105°$ which corresponds to one of the symmetry axes.

The robustness of our scheme was further tested by analyzing the partially occluded Pentagon image in Fig. 11(a), where a patch from the background of Fig. 9 was overlaid on the Pentagon image. The robustness of the MUSIC approach used for symmetry order estimation is exemplified in Fig. 9(b), where we accurately estimate the number of symmetry axes $N = 5$. We used a 2-D MUSIC scheme which provides better results than the four-dimensional scheme used in Fig. 10. Yet, our scheme failed to accurately estimate α_0 as two peaks can be identified in $\widetilde{g}_P(\theta)$ in Fig. 11(e). The highest peak results in $\alpha_0 = 4.7°$ which does not correspond to any of the symmetry axes. The second peak, which is located at $\widehat{\theta}_0 = 14.89°$, corresponds to the correct tilt angle of the occlusion-free case (Fig. 10). We conclude that the symmetry order estimation step of our scheme (using MUSIC) is more robust than the localization of the symmetry axes.

The proposed scheme was implemented in C++ and the computational time is about 20 s for a 256×256 image using a 2.8-GHz Pentium running WinXP. Profiling shows that 90% of the running time is related to the computation of the PPFT, whose implementation is currently not optimized. When properly implemented, the PPFT is slower than the 2-D FFT by only a small constant.

VII. Conclusion

We presented a 2-D symmetry detection algorithm which detects both rotational and reflectional symmetries. Our approach operates in the frequency domain by reformulating the symmetry detection as the analysis of a periodic signal embedded in noise, which is a classical signal processing problem with known and effective solutions. This formulation is based on computing the AC using the PPFT. It is shown to be algebraically accurate and effective in recovering both centered and noncentered symmetries.

Acknowledgment

The authors would like to thank Prof. M. Elad for his permission to reproduce Fig. 2(a). The authors would also like to thank the Associate Editor and the anonymous reviewers for their constructive feedback on an earlier version of this paper.

References

[1] M. A. Arbib, *The Handbook of Brain Theory and Neural Networks*. Cambridge, MA: MIT Press, 1995.

[2] A. Averbuch, D. L. Donoho, R. R Coifman, M. Israeli, and Y. Shkolnisky, "Fast slant stack: A notion of Radon transform for data in cartesian grid which is rapidly computable, algebraically exact, geometrically faithful and invertible," *SIAM Sci. Comput.*, to be published.

[3] S. Derrode and F. Ghorbel, "Robust and efficient Fourier–Mellin transform approximations for gray-level image reconstruction and complete invariant description," *Comput. Vis. Image Understand.*, vol. 83, no. 1, pp. 57–78, Jul. 2001.
[4] S. Derrode and F. Ghorbel, "Shape analysis and symmetry detection in gray-level objects using the analytical Fourier–Mellin representation," *Signal Process.*, vol. 84, no. 1, pp. 25–39, Jan. 2004.
[5] W. Kim and Y. Kim, "Robust rotation angle estimator," *IEEE Trans. Pattern Anal. Mach. Intell.*, vol. 21, no. 8, pp. 768–773, Aug. 1999.
[6] N. Kiryati and Y. Gofman, "Detecting symmetry in grey level images: The global optimization approach," in *Int. J. Comput. Vis.*, Aug. 1998, vol. 29, no. 1, pp. 29–45.
[7] C. D. Kuglin and D. C. Hines, "The phase correlation image alignment method," in *Proc. IEEE Conf. Cybernetics and Society*, Sep. 1975, pp. 163–165.
[8] L. Lucchese, "Frequency domain classification of cyclic and dihedral symmetries of finite 2-D patterns," *Pattern Recognit.*, vol. 37, pp. 2263–2280, 2004.
[9] W. Miller, *Symmetry Groups and their Applications*. London, U.K.: Academic, 1972.
[10] B. Porat, *A Course in Digital Signal Processing*. New York: Wiley, 1997.
[11] V. S. N. Prasad and B. Yegnanarayana, "Finding axes of symmetry from potential fields," *IEEE Trans. Image Process.*, vol. 13, no. 12, pp. 1559–1566, Dec. 2004.
[12] L. R. Rabiner, R. W. Schafer, and C. M. Rader, "The chirp z-transform algorithm," *IEEE Trans. Audio ElectroAcoust.*, vol. AU-17, no. 3, pp. 86–92, Jun. 1969.
[13] D. Reisfeld, H. Wolfson, and Y. Yeshurun, "Context free attentional operators: The generalized symmetry transform," *Int. J. Comput. Vis.*, pp. 119–130, 1995.
[14] D. Shen, H. Ip, and E. Teoh, "A novel theorem on symmetries of 2D images," in *Int. Conf. Pattern Recognit.*, Sep. 2000, vol. 3, pp. 1002–1005.
[15] D. Shen, H. Ip, and E. K. Teoh, "Robust detection of skewed symmetries by combining local and semi-local affine invariants," *Pattern Recognit.*, vol. 34, no. 7, pp. 1417–1428, 2001.
[16] P. N. SwarztrauberD. H. Bailey, "The fractional Fourier transform and applications," *SIAM Rev.*, vol. 33, no. 3, pp. 389–404, Sep. 1991.
[17] H. Weyl, *Symmetry*. Princeton, NJ: Princeton Univ. Press, 1952.
[18] H. Zabrodsky, S. Peleg, and D. Avnir, "Symmetry as a continuous feature," *IEEE Trans. Pattern Anal. Mach. Intell.*, vol. 17, no. 12, pp. 1154–1166, 1995.

Yosi Keller received the B.Sc. degree in electrical engineering from the Technion—Israel Institute of Technology, Haifa, in 1994 and the M.Sc. and Ph.D. degrees in electrical engineering from Tel Aviv University, Tel Aviv, Israel, in 1998 and 2003, respectively.

From 1994 to 1998, he was an R&D Officer with the Israeli Intelligence Force. He is currently a Visiting Assistant Professor with the Department of Mathematics, Yale University, New Haven, CT. His research interests include computer vision and statistical pattern analysis.

Yoel Shkolnisky received the B.Sc. degree in mathematics and computer science and the M.Sc. and Ph.D. degrees in computer science from Tel-Aviv University, Tel-Aviv, Israel, in 1996, 2001, and 2005, respectively.

He is a Gibbs Assistant Professor with the Department of Applied Mathematics, Yale University, New Haven, CT. His research interests include computational harmonic analysis and scientific computing.